EDGE ARTICLE

Check for updates

Iron tris-mesityl: a homoleptic iron(ii) ferrate species for directed C–H activation

Aleksa Radović, ID †[a] Maria C. Healy, ID †[b] Arnadeep Datta,[c] Deborshee Das, ID [c]
Likun Cai, ID [a] Steven Diaz, ID [a] Achyut Ranjan Gogoi,[c] Nikki J. Wolford,[a]
Stephanie H. Carpenter,[a] William W. Brenessel, ID [a] David McCamant, ID *[a]
Osvaldo Gutierrez ID *[c] and Michael L. Neidig ID *[b]

C–H activation is a vital synthetic tool due to its superior atom economy and improved step efficiency making it amendable to late-stage functionalisation. In recent years iron has been gaining traction within this field due to its high abundance, low cost and low toxicity. Iron(0) phosphines for C–H activation via oxidative addition are well documented, however, only a handful of iron(ii) complexes competent at C–H activation via ligand-to-ligand hydrogen atom transfer (LLHT) or σ-bond metathesis have been identified. Herein we report the first homoleptic iron species capable of facilitating C–H activation, introducing a new class of well-defined iron(ii) complexes for this purpose, and detail the synthesis and characterisation of a range of tris-cyclometalated iron complexes using a variety of pyridine derived substrates. Density functional theory (DFT) calculations reveal that the C–H activation proceeds through a σ-bond metathesis pathway.

Introduction

Transition metal-catalysed C–H bond activation is a powerful synthetic strategy for atom and step efficient synthesis across a range of substrates. This field has previously been dominated by precious metal catalysts, such as palladium, where both effective stoichiometric and catalytic reactions are well established.[1–3] Motivated by the goal to develop sustainable and environmentally friendly synthetic methods, there has been substantial interest in the development of first row transition metal catalysed C–H activation. Iron in particular is a highly attractive candidate for such reactions due to its low cost, limited toxicity and high abundance, yet current systems, including the breadth of iron complexes competent for C–H activation, remain underdeveloped compared to their precious metal analogues.[4–6]

Over the past 50 years, iron catalysts have been highly sought after to activate a variety of C–H bonds as a method of generating Fe–C bonded organometallic species that allow for subsequent functionalisation.[7–11] Historically, iron-catalysed C–H activation pathways have been classified into two general

categories: (1) C–H activation by oxidative addition to a low-valent iron complex to form both Fe–C and Fe–H bonds[10–23] and (2) σ-bond metathesis ligand-to-ligand hydrogen transfer mechanism (LLHT), commonly employing Fe(ii)–R complexes (R = amide, methyl, *etc.*) where the organic ligand acts as a base to remove the hydrogen from the substrate.[23–31] The chemistry of low-valent iron has been widely explored for C–H activation over the past few decades, including numerous studies utilising Fe(0)(dmpe)$_2$ (dmpe = 1,2-bis(dimethylphosphino)ethane), Fe(0)(dppe)$_2$ (dppe = 1,2-bis(diphenylphosphino)ethane) and Fe(0)(PMe$_3$)$_4$ complexes for both stoichiometric and catalytic C–H activation while more recent examples include Fe(0)–NHC (NHC = N-heterocyclic carbene) styrene complexes for stereoselective synthesis.[12–14,32] Additional approaches include the use of heterobimetallic species such as low-valent Fe–Al and Fe–Na complexes, as well as Fe(0)carbonyl complexes to facilitate C–H bond activation.[7,8,33–35]

By contrast, the development of well-defined Fe(ii)–R complexes capable of C–H activation via σ-bond metathesis/ LLHT has been less broadly explored. For example, half-sandwich Cp* complexes such as Cp*Fe(ii)PhL$_2$ (L = P(OR)$_3$) and Cp*Fe(CO)Ph(MeCN) have been demonstrated to C–H activate a variety of heteroaromatic substrates to generate metalated Fe(ii) products in a regioselective manner (Fig. 1).[24–26] Additional examples include FeMe$_2$(PMe$_3$)$_4$ for the formation of ferracycles from diphenylenimine and thiobenzophenones, as well as Fe(ii) amides that can activate aromatic C–H bonds to form organoiron products.[14,28] Despite these advances, it is clear that the overall understanding of C–H activation by Fe(ii)–R

aDepartment of Chemistry, University of Rochester, 120 Trustee Rd, Rochester, NY14627, USA

bDepartment of Chemistry, Inorganic Chemistry Laboratory, University of Oxford, South Parks Road, Oxford OX1 3QR, UK

cDepartment of Chemistry and Biochemistry, University of California, Los Angeles, 607 Charles E. Young Drive East, Los Angeles, CA, 90095, USA. E-mail: o.gutierrez@ucla.edu

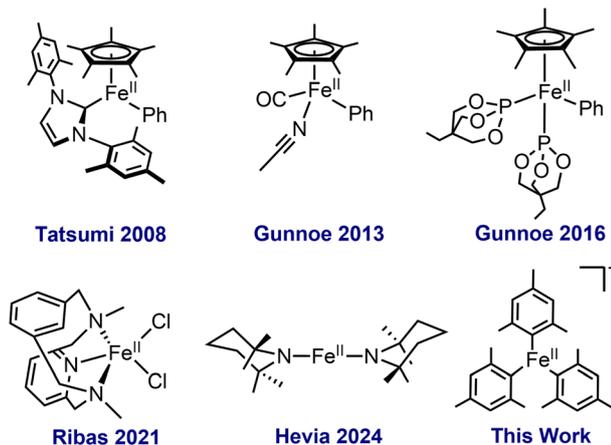† These authors contributed equally to this work.

Fig. 1 Examples of well-defined Fe(II) complexes for C–H activation.

complexes remains underdeveloped and the identification of new classes of Fe(II) complexes capable of efficient C–H activation is critical to broadening the synthetic utility of iron C–H activation chemistry.

Over the past decade, several studies have identified the importance of homoleptic organoferrate species in iron-catalysed cross-coupling reactions where they readily activate a variety of C–X bonds (X= Br, Cl).[36–40] Furthermore, recent mechanistic studies of directed C–H activation have implicated Fe(II)-aryl intermediates supported by bisphosphine ligands as key species for C–H activation.[41–43] Thus, we hypothesised that homoleptic Fe(II) organoferrate complexes would be able to activate stronger C–H bonds, enabling facile directed C–H activation without the need for complex and often expensive supporting ligands commonly employed in C–H activation methods. Herein we demonstrate that $[FeMes_3][MgBr(THF)_5]$ ($FeMes_3^-$) is efficient for directed C–H activation, identifying a new class of Fe(II) complexes for this reaction.

Results and discussion

C–H activation of benzo(*h*)quinoline with $FeMes_3^-$

We initiated our investigation of homoleptic iron species with $FeMes_3^-$, an easily synthesised and thermally stable homoleptic Fe(II) organoferrate, probing its C–H activation abilities by reaction of $FeMes_3^-$ (see SI for synthesis and isolation) with 3.1 equiv. of benzoquinoline (Hbzq), a common substrate for directed C–H activation with iron. After 6 hours at room temperature a colour change from pale yellow to dark green was observed. This reaction was investigated *via* 80 K ^{57}Fe Mössbauer, with the Mössbauer spectrum revealing only partial conversion of $FeMes_3^-$ to a new iron species **1** (7% conversion, see SI, Fig. S1). Heating the reaction to 60 °C for 1 hour led to the near complete consumption of $FeMes_3^-$ (Fig. 2: green trace, $\delta = 0.21$ mm s^{-1}, $|\Delta E_Q| = 1.43$ mm s^{-1}, 14% of iron) and formation of two new iron species: **1** (Fig. 2: blue trace, $\delta = 0.06$ mm s^{-1}, $|\Delta E_Q| = 0.71$ mm s^{-1}, 65% of iron) and **2** (Fig. 2: red trace, $\delta = 0.04$ mm s^{-1}, $|\Delta E_Q| = 1.95$ mm s^{-1}, 21% of iron). The same two iron species are also present after 3 hours,
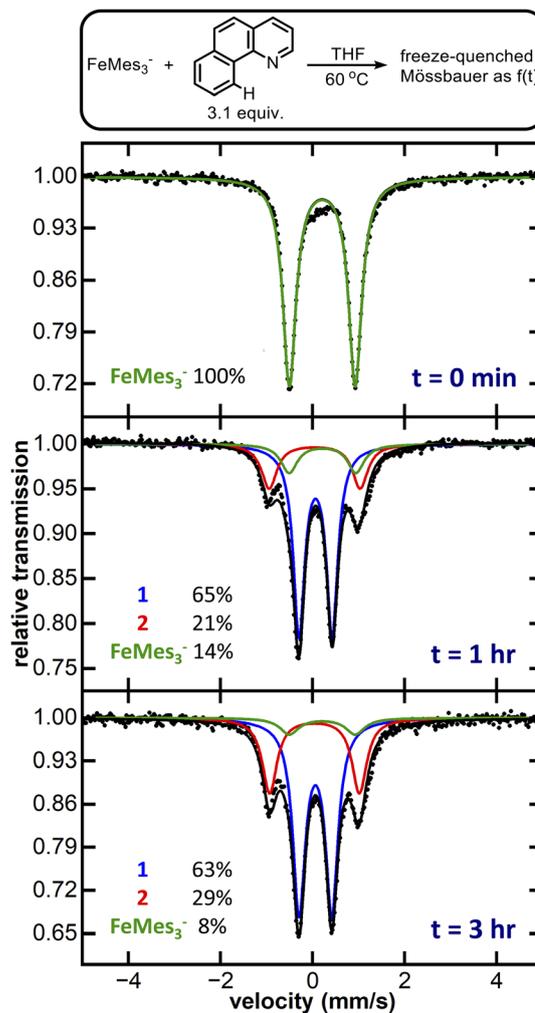

Fig. 2 Zero-field, 80 K ^{57}Fe Mössbauer spectra of $FeMes_3^-$ reacted with Hbzq at 60 °C. Black dotted trace: raw data. Solid black trace: best total fit. Coloured solid traces: simulation. Blue trace: **1** $\delta = 0.06$ $|\Delta E_Q| = 0.71$ mm s^{-1}. Red trace: **2** $\delta = 0.04$ $|\Delta E_Q| = 1.95$ mm s^{-1}. Green trace: $FeMes_3^-$ $\delta = 0.21$ $|\Delta E_Q| = 1.43$ mm s^{-1}.

comprising 92% of total iron. Performing the same reaction using *in situ* generated $FeMes_3^-$ formed from the reaction of FeBr$_2$ with 3.1 equiv. of MesMgBr yielded a similar mixture of **1** and **2** (see SI, Fig. S3). Note no reaction of MesMgBr with Hbzq is observed in the control reaction in the absence of iron (see SI, Fig. S19).

The observed reduction in isomer shifts for **1** and **2** compared to $FeMes_3^-$ (*i.e.* $\delta = 0.06$ mm s^{-1} for **1** *versus* 0.21 mm s^{-1} for $FeMes_3^-$) was suggestive of a significant ligation change to the iron centre, further corroborated by single crystal X-ray diffraction (SC-XRD). Crystallisation from the reaction mixture afforded two distinct crystals: purple-black needle-shaped crystals identified as the cyclometalated neutral homoleptic Fe(III) tris-(benzoquinolinyl) complex Fe(bzq)$_3$ (**2-bzq**) (Fig. 3) and green-black needle shaped crystals tentatively identified by SC-XRD as the Fe(II) tris-(benzoquinolinyl) complex, [Fe(bzq)$_3$][MgBr(THF)$_5$] however, crystals were poorly diffracting therefore no detailed discussion of the bond metrics is provided.
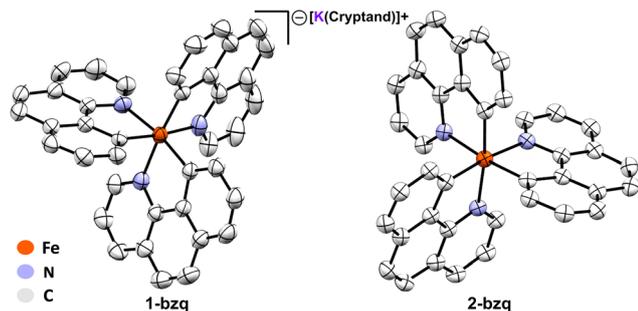
Fig. 3 Crystal structures of **1-bzq** and **2-bzq** as identified by SC-XRD. Hydrogen atoms and potassium 2,2,2-cryptand counterion of **1-bzq** omitted for clarity, thermal ellipsoids are shown at 50% probability. Selected average bond lengths (Å) and angles (°): **1-bzq** Fe–N 1.9983, Fe–C 1.9515, N–Fe–N 91.90 C–Fe–C 93.05, C–Fe–N$_{trans}$ 173.25, C–Fe–N 82.88. **2-bzq** Fe–N 2.0511, Fe–C 1.9545, N–Fe–N 90.88 C–Fe–C 94.98, C–Fe–N$_{trans}$ 173.02, C–Fe–N 82.62.

Observation of these two iron species is consistent with the species identified in the reaction by 80 K ^{57}Fe Mössbauer spectroscopy, where the component with the higher isomer shift and smaller quadrupole splitting (Fig. 2: blue trace, $\delta = 0.06$ mm s^{-1}, $|\Delta E_Q| = 0.71$ mm s^{-1}) can be attributed to the Fe(II) complex, while the second component (Fig. 2: red trace, $\delta = 0.04$ mm s^{-1}, $|\Delta E_Q| = 1.95$ mm s^{-1}) can be attributed to the Fe(III) complex **2-bzq**. The ^{13}C{^{1}H} NMR of the post reaction mixture confirmed the presence of mesitylene as the only organic by-product (see SI, Fig. S18).

To isolate substantial quantities of pure C–H activation products for characterisation, and to obtain a crystal structure of the Fe(II) tris-(benzoquinolinyl) complex, we sought to first isolate the Fe(III) complex, allowing for successive quantitative reduction to the Fe(II) complex. *In situ* formed **FeMes$_3$**$^-$ was reacted with Hbzq at 60 °C for 12 hours. Exposure of the reaction mixture to dry air at room temperature resulted in generation of the oxidised product **2-bzq** in 85% isolated yield. The 80 K ^{57}Fe Mössbauer spectrum of solid **2-bzq** shows parameters of $\delta = 0.04$ mm s^{-1} and $|\Delta EQ| = 1.95$ mm s^{-1} (Fig. 4, red trace), identical to those observed *in situ* for product **2** and further supporting its assignment as the C–H activated product **2-bzq**. The 10 K EPR spectrum of **2-bzq** exhibits an axial signal with $g_\parallel = 2.47$ and $g_\perp = 1.84$ (see SI, Fig. S6). The distribution of the g values indicates localisation of the unpaired electron on the metal d-orbital with little to no ligand radical character.

Subsequent reduction of isolated **2-bzq** with 1 equiv. of KC$_8$ and 2,2,2-cryptand in acetonitrile (MeCN) at room temperature gave the reduced complex [Fe(bzq)$_3$][K(2,2,2-cryptand)] (**1-bzq**) in 56% isolated yield. Crystals suitable for SC-XRD were obtained by vapour diffusion with diethyl ether, verifying the structure of **1-bzq** as the Fe(II) ate analogue of **2-bzq** (Fig. 3). The 80 K ^{57}Fe Mössbauer spectrum of solid **1-bzq** is characterised by $\delta = 0.06$ mm s^{-1} and $|\Delta E_Q| = 0.65$ mm s^{-1} (Fig. 4, blue trace), consistent with the assignment of *in situ* formed **1** as the Fe(II) C–H activated product **1-bzq**. The ^{1}H NMR spectrum of **1-bzq** did not display any broadened or paramagnetic signals associated with paramagnetic iron species, indicating that **1-bzq** is
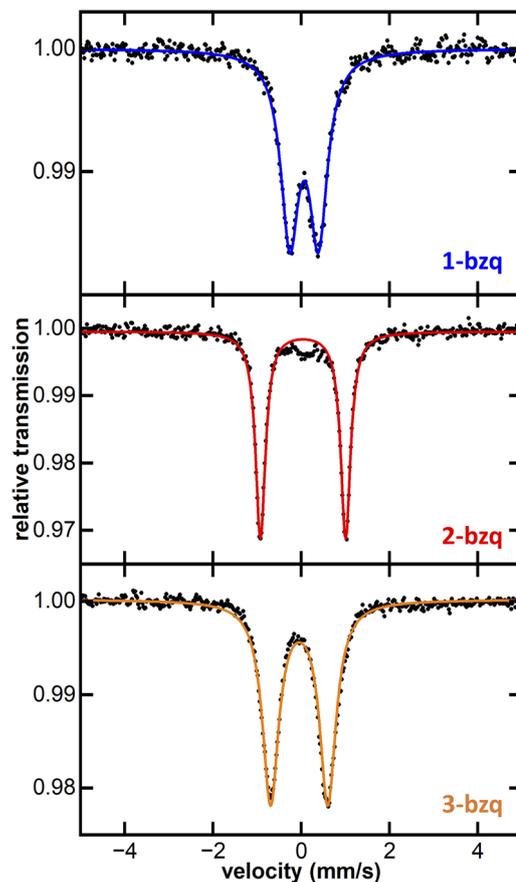

Fig. 4 Zero-field, solid 80 K ^{57}Fe Mössbauer spectra of isolated complexes **1-bzq**, **2-bzq** and **3-bzq**. Black dotted trace: raw data. Coloured solid traces: simulation. **1-bzq** $\delta = 0.06$ $|\Delta E_Q| = 0.65$ mm s^{-1}. **2-bzq** $\delta = 0.04$ $|\Delta E_Q| = 1.95$ mm s^{-1}. **3-bzq** $\delta = -0.05$ $|\Delta E_Q| = 1.30$ mm s^{-1}.

a diamagnetic low-spin Fe(II) complex (see SI, Fig. S20). Overall, these results suggest that **1-bzq** is initially formed from three successive C–H activations of **FeMes$_3$**$^-$ and is subsequently oxidised to **2-bzq** by trace oxygen *in situ*, consistent with facile oxidation due to the increased σ-donor properties of these cyclometalating ligands. This coincides with cyclic voltammetry (CV) studies carried out on **1-bzq** in MeCN *vs.* a ferrocene standard (see SI, Fig. S7) which indicated the presence of two reversible redox couples with $E_{1/2} = -1.66$ V and -0.34 V *vs.* Fc/Fc$^+$ assigned to Fe(II)/Fe(III) and Fe(III)/Fe(IV) redox couples respectively. The cyclic voltammogram of **2-bzq** in DCM *vs.* Fc/Fc$^+$ yielded similar results with two reversible redox couples observed with $E_{1/2} = -1.83$ V and -0.48 V *vs.* Fc/Fc$^+$, again attributed to Fe(II)/Fe(III) and Fe(III)/Fe(IV) respectively (see SI Fig. S8).

Given that the CV studies indicated a reversible and accessible Fe(III)/Fe(IV) couple, we attempted to complete an isostructural series comprising Fe(II), Fe(III) and Fe(IV) analogues, by reacting **2-bzq** with 1 equiv. of cerium ammonium nitrate at room temperature in MeCN, successfully generating the Fe(IV) tris-cyclometalated analogue **3-bzq** (SC-XRD in SI, Fig. S42). The 80 K ^{57}Fe Mössbauer spectrum of solid **3-bzq** has parameters of

$\delta = -0.05$ mm s^{-1} and $|\Delta E_{\mathrm{Q}}| = 1.30$ mm s^{-1} (Fig. 4, orange trace). The decreased isomer shift of **3-bzq** compared to **2-bzq** is consistent with the formation of a paramagnetic $S = 1$ Fe(IV) complex.

Directed C–H activation with FeMes$_3$$^-$

Having established that **FeMes$_3$$^-$** can C–H activate Hbzq, we next probed the viability of this synthetic procedure with a wider set of pyridine-derived directed substrates. 2-Phenylpyridine (Hppy), 2-(p-tolyl)pyridine (Hptpy) and 2-(2,4-difluorophenyl) pyridine (Hdfppy) were selected to evaluate the influence of the ligand π system and electron donating/withdrawing groups on C–H activation by **FeMes$_3$$^-$**. Fe(III) products were targeted using subsequent treatment of C–H activated product solution with dry air as previously described. Utilising this procedure, tris-cyclometalated Fe(III) complexes Fe(ppy)$_3$ (**2-ppy**), Fe(ptpy)$_3$ (**2-ptpy**), and Fe(dfppy)$_3$ (**2-dfppy**) were also synthesised and structurally characterised by SC-XRD (Fig. 5). The 10 K EPR spectra of complexes **2-ppy**, **2-ptpy**, and **2-dfppy** indicated that all of the Fe(III) tris-cyclometalated products are low-spin $S = 1/2$ complexes based upon the observed axial EPR spectra and associated g-values observed (and further supported by ^{57}Fe 80 K Mössbauer spectroscopy) (Table 1).

2-ppy, **2-ptpy** and **2-dfppy** could be easily reduced with potassium graphite at room temperature to generate the Fe(II) analogues **1-ppy**, **1-ptpy**, and **1-dfppy** as confirmed by SC-XRD ^{57}Fe 80 K Mössbauer spectroscopy (see SI, Fig. S38–S41).

3-Methyl-2-phenylpyridine (Hmppy) and 2-(2,4-difluorophenyl)-5-fluoropyridine (Hdfpfpy) could also be employed to isolate crystals of Fe(mppy)$_3$ (**2-mppy**) and

Table 1 80 K ^{57}Fe Mössbauer and 10 K EPR parameters of Fe(III) tris-cyclometalated complexes

Complex	Mössbauer parameters		EPR parameters	
	δ (mm s^{-1})	$|\Delta E_{\mathrm{Q}}|$ (mm s^{-1})	$g_{\parallel}$	$g_{\perp}$
2-bzq	0.04	1.93	2.47	1.84
2-ppy	−0.01	1.82	2.42	1.90
2-ptpy	0.01	1.82	2.46	1.87
2-dfppy	−0.01	1.83	2.46	2.00

Fe(dfpfpy)$_3$ (**2-dfpypy**) for SC-XRD analysis (Fig. 5), though the use of these substrates gave very poor synthetic yields that did not permit further characterization or reduction attempts of the product complexes.

Mechanism of directed C–H activation by FeMes$_3$$^-$

The ability of **FeMes$_3$$^-$** to efficiently perform directed C–H activation of Hbzq (>90% solution yield of tris-cyclometalated products identified by freeze-trapped 80 K ^{57}Fe Mössbauer spectroscopy) represents a new reactivity for this simple homoleptic ferrate. While the observation of mesitylene as the organic product of this reaction is suggestive of C–H activation via σ-bond metathesis or a ligand-to-ligand hydrogen transfer (LLHT) mechanism, we sought to further explore the intermediates involved in the formation of **1-bzq**. As three successive C–H activations are required to form this product, we first sought to identify the iron product after the first C–H activation. To achieve this, **FeMes$_3$$^-$** was reacted with 1 equiv. of Hbzq at 60 °C in THF (the previously identified reaction conditions for C–H activation). 80 K ^{57}Fe Mössbauer spectroscopy of the reaction freeze-trapped after 3 hours contained both tris-cyclometalated product **1-bzq** (27% of total iron by Mössbauer) and unreacted **FeMes$_3$$^-$** (63% of total iron by Mössbauer) (see SI, Fig. S2). This result is consistent with the first C–H activation being the rate determining step of the three C–H activation steps involved in formation of **1-bzq**, and resulting in no iron intermediates after the first and second C–H activations being observable in situ.

To probe the mechanistic manifold of this process, we employed dispersion-corrected density functional theory (DFT) at the UB3LYP-D3/def2-SVP-CPCM(THF)//UB3LYP-D3/6-31-G(d)-CPCM(THF) level of theory (Fig. 6a). The calculations indicate that **FeMes$_3$$^-$** and Hbzq initially associate to form **Int-bzq1** that allows for subsequent C(sp^2)–H activation of Hbzq via transition state **TS1** with an energy barrier of 29.4 kcal mol^{-1} (with respect to **Int-bzq1** from IRC calculations), yielding the intermediate **Int-1**. This intermediate undergoes subsequent C–H activation via **TS2** and **TS3** to afford the final product **1-bzq** (Fig. 6). The second C–H activation barrier via **TS2** is comparable with the initial C–H activation via **TS1**. The third C–H activation barrier via **TS3** is notably lower than both the first and second C–H activation steps. Each C–H activation step generates a progressively lower energy intermediate from the tri-coordinated **FeMes$_3$$^-$** complex. Thus, we hypothesize that
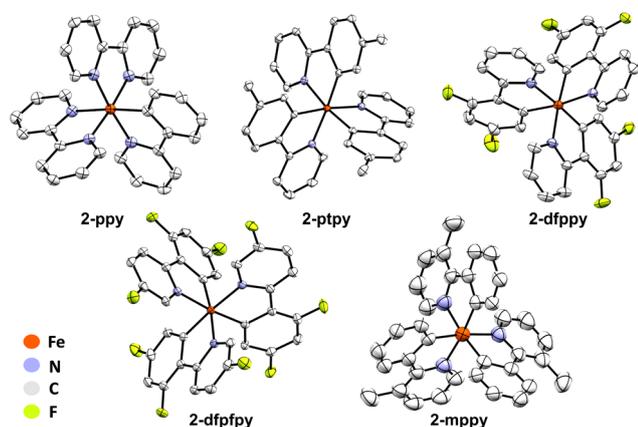

Fig. 5 Crystal structures of Fe(III) complexes **2-ppy**, **2-ptpy**, **2-dfppy**, **2-dfpfpy** and **2-mppy** as identified by SC-XRD. Hydrogen atoms and solvent molecules omitted for clarity. Thermal ellipsoids are shown at 50% probability. Selected average bond lengths (Å) and angles (°): **2-ppy** Fe–N 2.0090, Fe–C 1.9780, N–Fe–N 95.62, C–Fe–C 93.76, C–Fe–N$_{trans}$ 174.76, C–Fe–N 81.68. **2-ptpy** Fe–N 2.0357, Fe–C 1.9529, N–Fe–N 93.80, C–Fe–C 93.55, C–Fe–N$_{trans}$ 173.98, C–Fe–N 82.15. **2-dfppy** Fe–N 2.0252, Fe–C 1.9500, N–Fe–N 94.38 C–Fe–C 93.88, C–Fe–N$_{trans}$ 174.93, C–Fe–N 82.04. **2-dfpfpy** Fe–N 2.0223, Fe–C 1.9490, N–Fe–N 94.48, C–Fe–C 93.74, C–Fe–N$_{trans}$ 174.49, C–Fe–N 82.03. **2-mppy** Fe–N 2.0360, Fe–C 1.9436, N–Fe–N 94.48, C–Fe–C 94.84, C–Fe–N$_{trans}$ 173.44, C–Fe–N 80.85.
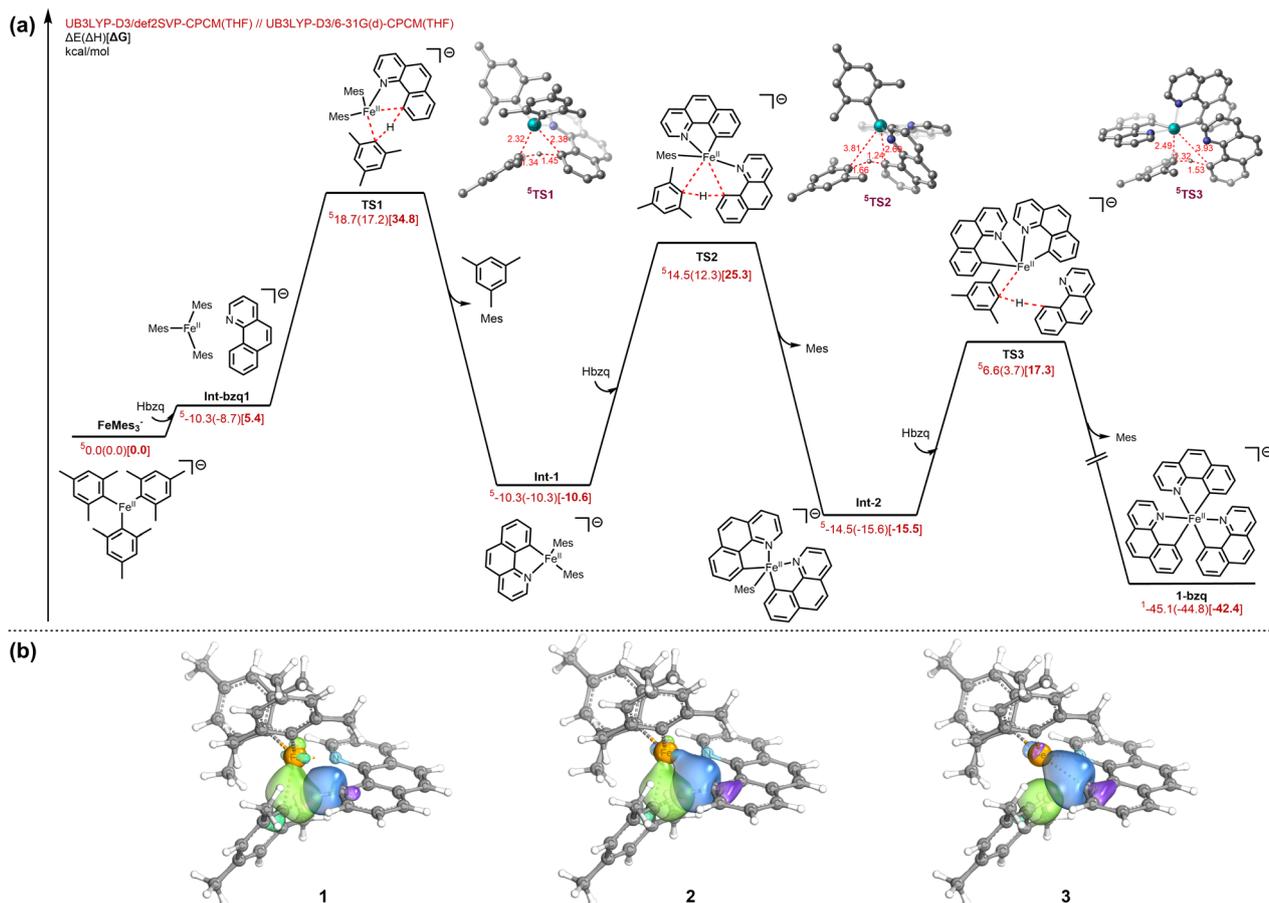
Fig. 6 (a) Computational investigation into the full sp^2 C–H activation pathway with associated transition states (TS1, TS2 & TS3) in lowest energy spin state. (b) Intrinsic bond orbital analysis of the associated σ-bond metathesis sp^2 C–H activation step, 1 (stationary point from backward IRC of TS1), 2 (TS1), and 3 (stationary point from forward IRC of TS1). Multiplicities are in superscripts.

the formation of the more favourable octahedral complex **1-bzq** is thermodynamically driven. Previous examples of similar C–H activation systems are reported to proceed *via* a σ-bond metathesis mechanism[6,43,44] or LLHT where the iron centre is participating in the hydride transfer process.[31] To differentiate between a LLHT process and a σ-bond metathesis mechanism, we performed intrinsic bond orbital (IBO) analysis (Fig. 6b) to trace the electron flow in **TS1** from **1** (stationary point from backward IRC of **TS1**), **2** (**TS1**), and **3** (stationary point from forward IRC of **TS1**).

The analysis reveals the concerted participation of four distinct σ-bonds (mesityl_C–H, Hbzq_C–H, Fe–C_mesityl, and Fe–C_Hbzq) in the transition state. Crucially, unlike oxidative addition, the electron pair in the Fe–C_mesityl σ-bond is utilized to accommodate the transferring proton effectively forming a new mesityl_C–H bond rather than involving electron density from the iron d-orbitals. In this instance, IBO analysis characterizes the mechanism as a formal [2σ + 2σ] σ-bond metathesis process,[45] rather than metal d-assisted σ-bond metathesis or LLHT mechanism. Therefore, while the Fe–N interaction is crucial for achieving the appropriate geometry required for the C–H activation transition state, the iron centre

itself does not exhibit direct orbital involvement in the hydride transfer at the transition state.

Excited state properties of tris-cyclometalated iron complexes

Beyond the synthetic impact of identifying **FeMes$_3^-$** as a new complex for directed C–H activation reactions, the tris-cyclometalated iron products accessible in this reaction are also of interest with respect to the field of iron photoredox catalysis. There has been broad interest in the photophysics and excited state lifetimes of cyclometalated iron complexes across a variety of iron oxidation states. Therefore, we employed ultrafast transient absorption (TA) spectroscopy to probe the excited state properties of **1-bzq**, **2-bzq** and **3-bzq** as representative examples of this class of tris-cyclometalated products. In addition to characterising the excited-state lifetimes of these species, the comparison of the transient spectra to those of the oxidised or reduced species can help identify the absorption band as either MLCT or LMCT in character.

The excited state absorption spectrum of **1-bzq** in MeCN (800 nm excitation to match the lowest energy charge transfer transition for the complex) shows an excited state absorption feature around 550 nm, while broad ground state bleach can be
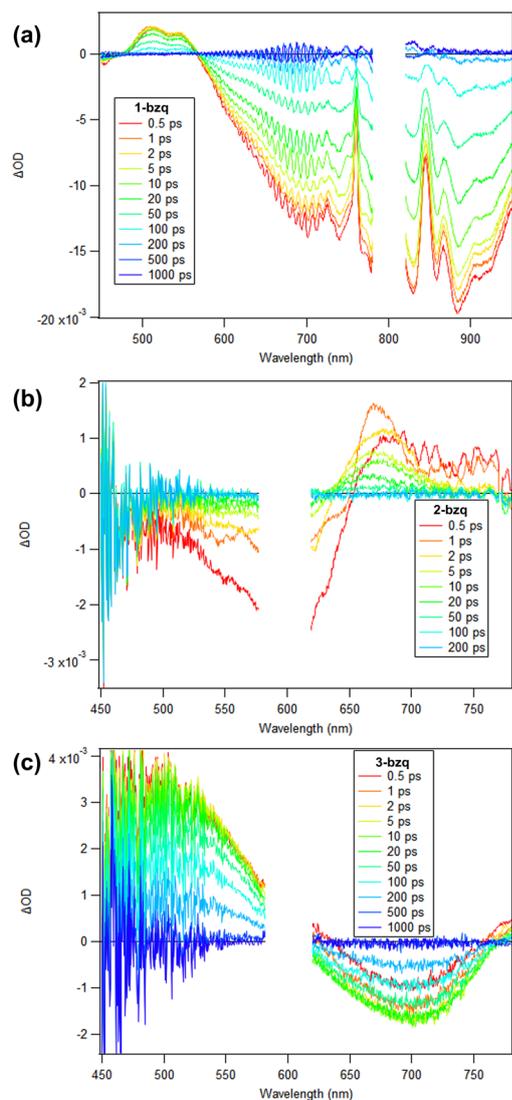
Fig. 7 (a) Transient absorption spectra of **1-bzq** in MeCN. (b) Transient absorption spectra of **2-bzq** in DCM. (c) Transient absorption spectra of **3-bzq** in MeCN. **2-bzq** and **3-bzq** were excited at 600 nm and **1-bzq** was excited at 800 nm. The sharp features from 700–900 nm in (a) are artifacts from the spectral shape of the white-light continuum.

observed between 600 and 1000 nm (Fig. 7a). The TA kinetics can be fit to two exponential functions with 3 ps excited-state reorganization process and a 56 ps excited state lifetime (Fig. S27, Table S1). Excitation to the CT band should lead to the formation of a ¹MLCT state which should rapidly undergo intersystem crossing to ³MLCT state, where absorption of this state should resemble the absorption spectrum of the oxidised, Fe(III) complex. Comparison of the excited state spectrum with the difference spectrum of the Fe(III)–Fe(II) complexes (Fig. S16) reveals good agreement between difference spectrum and longer-lived component, which suggests that longer lived excited state corresponds to the ³MLCT state. Additionally, the lack of any long-lived bleach in Fig. 7a indicates that **1-bzq** does not relax into a long-lived low-energy high spin state as [Fe^II(bpy)₃]²⁺ does.[46]

The excited state absorption (ESA) spectrum of **2-bzq** in DCM (600 nm excitation corresponding to the lowest energy charge-transfer transition of the complex) shows only weak features around 670–760 nm, just to longer wavelengths relative to the ground-state absorption band, while broad ground-state bleach (GSB) can be observed between 550 and 650 nm (Fig. 7b). The dynamics can be fit with excited state lifetime of 0.33 ps (see SI, Fig. S27). Then, on the 10 ps time scale we observe the vibrational cooling of a hot ground-state species created by the ultrafast internal conversion to the ground state, which is apparent in the gradual shift of the peak of the ESA band from 670 to 655 nm on this time scale. Excitation to the CT band should lead to the formation of either a ²MLCT or a ²LMCT state, where absorption of this state should resemble the absorption spectrum of the oxidized Fe(IV) complex (for the MLCT transition) or the reduced, Fe(II) complex (for the LMCT transition). Comparison of the excited state spectrum with the difference spectrum of the Fe(IV) and Fe(III) complexes and the Fe(III) and Fe(II) complexes reveals better agreement with the Fe(IV)–Fe(III) difference spectrum which suggests that the observed excited state likely corresponds to the ²MLCT state (see SI, Fig. S15–S18). While both difference spectra would predict a broad ESA from 650–800 nm, only the Fe(IV)–Fe(III) difference predicts a significant bleach from 450–650 nm. Such short excited state lifetime is significantly lower compared to the Fe(III) complexes with NHC based ligands, which exhibit excited state lifetimes of 100 ps for [Fe(btz)₃]³⁺ and 2 ns for [Fe(phtmeimb)₂]⁺. This suggests that in the case of the **2-bzq** complex the energy difference between excited CT and an excited metal centred state is not sufficient to suppress non-radiative decay from this state.

Lastly, the excited state absorption spectrum of **3-bzq** shows a broad ESA feature spanning <450 nm to 600 nm, while a broad GSB can be observed from 620–760 nm (Fig. 7c). The excited state kinetics are fit to reveal an excited state lifetime of ~161 ps (see SI, Fig. S27). Excitation to the Fe(IV) CT band should lead to the formation of ³LMCT state, where absorption of this state should resemble the absorption spectrum of the Fe(III) complex. The excited state spectrum and difference spectrum of Fe(IV)–Fe(III) complexes (see SI, Fig. S14) are in good agreement suggesting that observed excited state corresponds to the ³LMCT state. This excited charge transfer state is significantly longer lived compared to the Fe(II) and Fe(III) complexes, indicating that Fe(IV) complexes may be good alternative to Fe(II) and Fe(III) complexes in photochemical applications. Notably, it is significantly longer lived compared to the previously characterised homoleptic Fe(IV) complexes (0.8 ps for [Fe(phtmeimb)₂]²⁺ and 1.4 ps for [Fe(ImP)₂]²⁺).[47,48]

A complete transient absorption characterisation of the excited state lifetimes of **1-ppy**, **2-ppy**, **1-ptpy**, **2-ptpy**, **1-dfppy** and **2-dfppy** is presented in the SI (Fig. S26, S28 and S29).

Conclusions

In this work, a new Fe(II) species competent at directed C–H activation has been identified allowing for the development of a simple synthetic method using easily accessible iron salt,

MesMgBr and a pyridine derived ligand precursor for directed C–H activation. DFT calculations revealed that transition state for the C–H activation process goes through a formal [2σ + 2σ] σ-bond metathesis pathway without any interaction with the iron centre. It is demonstrated that this method enables access to a wide variety of tris-cyclometalated iron complexes that have historically been synthetically challenging to access. This new class of iron complexes for C–H activation may enable new routes to functionalised products using sustainable iron catalysts.

Author contributions

A. R., M. C. H., N. J. W. and S. H. C. provided the experimental/spectroscopic data. A. D., D. D., A. R. G. and O. G. provided the computational data. A. D. and D. D. contributed equally to the computational studies. L. C. and S. D. collected and analysed transient absorption data. M. L. N., O. G. and D. McC. supervised this work. A. R., M. C. H. and M. L. N. prepared the original draft, all authors contributed to subsequent drafts.

Conflicts of interest

There are no conflicts to declare.

Data availability

The data supporting the findings of this study are available within the paper and its supplementary information (SI). Supplementary information: synthetic and experimental procedures, additional spectroscopic data, SC-XRD data and DFT calculations. See DOI: https://doi.org/10.1039/d5sc08832a.

Acknowledgements

Notes and references

1 X. Chen, K. M. Engle, D. H. Wang and J. Q. Yu, Angew. Chem., Int. Ed., 2009, 48, 5094–5115.

2 J. He, M. Wasa, K. S. Chan, Q. Shao and J.-Q. Yu, Chem. Rev., 2016, 117, 8754.

3 T. W. Lyons and M. S. Sanford, Chem. Rev., 2010, 110, 1147–1169.

4 M. L. Neidig, S. H. Carpenter, D. J. Curran, J. C. DeMuth, V. E. Fleischauer, T. E. Iannuzzi, P. G. N. Neate, J. D. Sears and N. J. Wolford, Acc. Chem. Res., 2019, 52, 140–150.

5 A. Fürstner, ACS Cent. Sci., 2016, 2, 778–789.

6 R. Shang, L. Ilies and E. Nakamura, Chem. Rev., 2017, 117, 9086–9139.

7 M. M. Bagga, P. L. Pauson, F. J. Preston and R. I. Reed, Chem. Commun., 1965, 543–544, DOI: 10.1039/C19650000543.

8 P. E. Baikie and O. S. Mills, Chem. Commun., 1966, 707–708, DOI: 10.1039/C19660000707.

9 W. Hübel and E. H. Braye, J. Inorg. Nucl. Chem., 1959, 10, 250–268.

10 G. Cerveau, E. Colomer and R. Corriu, J. Organomet. Chem., 1977, 136, 349–353.

11 M. V. Baker and L. D. Field, J. Am. Chem. Soc., 1986, 108, 7433–7434.

12 S. Ittel, C. Tolman, A. English and J. Jesson, J. Am. Chem. Soc., 1978, 100, 7577–7585.

13 C. Tolman, S. Ittel, A. English and J. Jesson, J. Am. Chem. Soc., 1979, 101, 1742–1751.

14 S. Camadanli, R. Beck, U. Flörke and H.-F. Klein, Organometallics, 2009, 28, 2300–2310.

15 G. Hata, H. Kondo and A. Miyake, J. Am. Chem. Soc., 1968, 90, 2278–2281.

16 M. K. Whittlesey, R. J. Mawby, R. Osman, R. N. Perutz, L. D. Field, M. P. Wilkinson and M. W. George, J. Am. Chem. Soc., 1993, 115, 8627–8637.

17 H. Azizian and R. H. Morris, Inorg. Chem., 1983, 22, 6–9.

18 S. D. Ittel, C. A. Tolman, P. J. Krusic, A. D. English and J. P. Jesson, Inorg. Chem., 1978, 17, 3432–3438.

19 M. Antberg and L. Dahlenburg, Z. Naturforsch., B, 1987, 42, 435–440.

20 H. H. Karsch, H. F. Klein and H. Schmidbaur, Chem. Ber., 1977, 110, 2200–2212.

21 M. V. Baker and L. D. Field, Organometallics, 1986, 5, 821–823.

22 M. V. Baker and L. D. Field, J. Am. Chem. Soc., 1987, 109, 2825–2826.

23 G. Xu, H. Sun and X. Li, Organometallics, 2009, 28, 6090–6095.

24 Y. Ohki, T. Hatanaka and K. Tatsumi, J. Am. Chem. Soc., 2008, 130, 17174–17186.

25 S. E. Kalman, A. Petit, T. B. Gunnoe, D. H. Ess, T. R. Cundari and M. Sabat, Organometallics, 2013, 32, 1797–1806.

26 K. H. Taylor, S. E. Kalman, T. B. Gunnoe and M. Sabat, Organometallics, 2016, 35, 1978–1985.

27 C. Magallón, O. Planas, S. Roldan-Gomez, J. M. Luis, A. Company and X. Ribas, Organometallics, 2021, 40, 1195–1200.

28 A. Logallo, L. C. Maddock, M. Mu, L. Gravogl, N. Jin, M. N. Peñas-Defrutos, K. Meyer, M. García-Melchor and E. Hevia, Angew. Chem., Int. Ed., 2024, 63, e202402907.

29 S. H. Wunderlich and P. Knochel, Angew. Chem., Int. Ed., 2009, 48, 9717–9720.

30 P. Alborés, L. M. Carrella, W. Clegg, P. García-Álvarez, A. R. Kennedy, J. Klett, R. E. Mulvey, E. Rentschler and L. Russo, Angew. Chem., 2009, 121, 3367–3371.

31 S. Cattani, N. K. Pandit, M. Buccio, D. Balestri, L. Ackermann and G. Cera, Angew. Chem., 2024, 136, e202404319.

32 J. Cheng, Q. Chen, X. Leng, S. Ye and L. Deng, Inorg. Chem., 2019, 58, 13129–13141.

33 N. Gorgas, A. J. P. White and M. R. Crimmin, *J. Am. Chem. Soc.*, 2022, **144**, 8770–8777.

34 A. Tortajada and E. Hevia, *ACS Org. Inorg. Au*, 2025, **5**, 62–68.

35 T. Jia, C. Zhao, R. He, H. Chen and C. Wang, *Angew. Chem., Int. Ed.*, 2016, **55**, 5268–5271.

36 R. B. Bedford, P. B. Brenner, E. Carter, P. M. Cogswell, M. F. Haddow, J. N. Harvey, D. M. Murphy, J. Nunn and C. H. Woodall, *Angew Chem. Int. Ed. Engl.*, 2014, **53**, 1804–1808.

37 S. L. Daifuku, M. H. Al-Afyouni, B. E. Snyder, J. L. Kneebone and M. L. Neidig, *J. Am. Chem. Soc.*, 2014, **136**, 9132–9143.

38 S. B. Muñoz III, S. L. Daifuku, J. D. Sears, T. M. Baker, S. H. Carpenter, W. W. Brennessel and M. L. Neidig, *Angew. Chem.*, 2018, **130**, 6606–6610.

39 S. H. Carpenter, T. M. Baker, S. B. Muñoz, W. W. Brennessel and M. L. Neidig, *Chem. Sci.*, 2018, **9**, 7931–7939.

40 C. L. Sun, H. Krause and A. Fürstner, *Adv. Synth. Catal.*, 2014, **356**, 1281–1291.

41 T. E. Boddie, S. H. Carpenter, T. M. Baker, J. C. DeMuth, G. Cera, W. W. Brennessel, L. Ackermann and M. L. Neidig, *J. Am. Chem. Soc.*, 2019, **141**, 12338–12345.

42 J. C. DeMuth, Z. Song, S. H. Carpenter, T. E. Boddie, A. Radovic, T. M. Baker, O. Gutierrez and M. L. Neidig, *Chem. Sci.*, 2021, **12**, 9398–9407.

43 J. Mo, A. M. Messinis, J. Li, S. Warratz and L. Ackermann, *Acc. Chem. Res.*, 2024, **57**, 10–22.

44 C. E. Webster, Y. Fan, M. B. Hall, D. Kunz and J. F. Hartwig, *J. Am. Chem. Soc.*, 2003, **125**, 858–859.

45 Y.-H. Cheng, Y.-S. Ho, C.-J. Yang, C.-Y. Chen, C.-T. Hsieh and M.-J. Cheng, *J. Phys. Chem. A*, 2024, **128**, 4638–4650.

46 T. K. Ekanayaka, K. P. Maity, B. Doudin and P. A. Dowben, *Nanomaterials*, 2022, **12**(10), 1742.

47 J. Steube, L. Fritsch, A. Kruse, O. S. Bokareva, S. Demeshko, H. Elgabarty, R. Schoch, M. Alaraby, H. Egold, B. Bracht, L. Schmitz, S. Hohloch, T. D. Kühne, F. Meyer, O. Kühn, S. Lochbrunner and M. Bauer, *Inorg. Chem.*, 2024, **63**, 16964–16980.

48 O. Prakash, P. Chábera, N. W. Rosemann, P. Huang, L. Häggström, T. Ericsson, D. Strand, P. Persson, J. Bendix and R. Lomoth, *Chem.–Eur. J.*, 2020, **26**, 12728–12732.